Solar Energy Materials & Solar Cells 132 (2015) 47–55

Contents lists available at ScienceDirect

Solar Energy Materials & Solar Cells

journal homepage: www.elsevier.com/locate/solmat

Enhanced power conversion efficiency of dye-sensitized solar cells with multifunctional photoanodes based on a three-dimensional TiO_2 nanohelix array

Seung Hee Lee [a], Jeong Kwon [b], Dong Yeong Kim [a], Kyung Song [a], Sang Ho Oh [a], Jaehee Cho [c], E. Fred Schubert [d], Jong Hyeok Park [b,*], Jong Kyu Kim [a,**]

[a] Department of Materials Science and Engineering, Pohang University of Science and Technology (POSTECH), Pohang 790-784, Republic of Korea
[b] School of Chemical Engineering and SKKU Advanced Institute of Nano Technology (SAINT), Sungkyunkwan University, Suwon 440-746, Republic of Korea
[c] Department of Semiconductor Science and Technology, Chonbuk National University, Jeonju 561-756, Republic of Korea
[d] Electrical, Computer and Systems Engineering Department, Rensselaer Polytechnic Institute, Troy, NY 12180, USA

ARTICLE INFO

Article history:
Received 2 July 2014
Received in revised form
1 August 2014
Accepted 6 August 2014

Keywords:
Dye-sensitized solar cell
Titanium dioxide nanohelix
Oblique angle deposition
Multifunctional photoanode
Nanoparticle infiltration

ABSTRACT

Developments of metal oxide nanostructures for simultaneous improvements in light harvesting and charge collection can lead to a significant technical progress in various applications such as photoelectrodes for photoelectrochemical cells and various types of solar cells. Here we present an array of three-dimensional titanium dioxide (TiO_2) nanohelixes infiltrated with TiO_2 nanoparticles as a multifunctional photoanode for dye sensitized solar cells (DSSCs). The unique geometry and the near-single crystallinity of the vertically aligned TiO_2 nanohelix array results simultaneously in strong light scattering and enhanced carrier transport and collection, while maintaining a comparable surface area accessible for dye molecules by the infiltrated TiO_2 nanoparticles. Consequently, despite a ~40% reduction in dye loading, the overall photon conversion efficiency of the DSSC with the nanoparticle-infiltrated nanohelix-array photoanode is enhanced by 6.2% in comparison with the DSSC with the conventional nanoparticle photoanode.

1. Introduction

Dye sensitized solar cells (DSSCs) have received great attention as one of the potential replacements for conventional solar cells due to their cost-effectiveness and ease of fabrication [1–5]. Recently, the record power conversion efficiency (PCE) of greater than 12% has been obtained [6], which may satisfy the requirements of most applications, yet leaves a room for further improvement towards the theoretical maximum PCE of ~20% [7]. Two strategies are typically considered for improving the PCE of solar cells: (i) improving the light harvesting efficiency to increase the number of photo-generated carriers, and (ii) promoting the charge collection that is determined by two competing processes – the transport and the recombination of the photo-generated carriers. However, there is a trade-off between the light harvesting and the charge collection efficiencies in general, which may require unsatisfactory compromises when designing an optimized solar cell.

Optical, electrical, and structural properties of photoelectrodes can strongly affect light harvesting as well as charge collection processes in various optoelectronic devices including photoelectrochemical cells, organic photovoltaics, and DSSCs. Especially in DSSCs, the geometry of a photoanode determines the amount of dye molecules accessible to the photoanode, as well as the scattering of incident light, thus affecting the overall light harvesting efficiency. In addition, the charge collection efficiency is strongly influenced by the micro-structural properties of the photoanode, *i.e.* whether the photoanode can provide photo-generated carriers with "express ways" for efficient transport with little recombination loss. Sintered networks of TiO_2 mesoporous nanoparticles (NP) have been widely used as photoanodes for conventional DSSCs due to their large surface area enabling adsorption of large amount of dye molecules for efficient light harvesting. However, light scattering is negligible because the size of typical NPs (about 10–20 nm) is much smaller than the wavelengths of solar spectrum [8], which calls for a thick photoanode to enable sufficient light absorption. On the other hand, entangled complex networks of sintered NPs with numerous grain boundaries obstruct efficient transport of the photo-generated carriers [9–12], which makes a thin photoanode desirable. One dimensional nanostructures such as arrays of nanowires [13–16],

* Corresponding author.
** Corresponding author.
E-mail addresses: lutts@skku.edu (J.H. Park), kimjk@postech.ac.kr (J.K. Kim).

http://dx.doi.org/10.1016/j.solmat.2014.08.007
0927-0248/

nanorods [11,17,18] or nanotubes [19–22] have been introduced to promote charge collection by providing direct electron pathways with reduced number of grain boundaries [19]. However, the PCE of the DSSCs with such photoanodes remains lower than that of conventional DSSCs due to a limited light harvesting caused by the much small surface area and little light scattering. Recently, combinations of one-dimensional nanostructures with NPs and hierarchically structured nanotubes or nanowires were reported to improve the dye loading capacity, and thus light harvesting, while maintaining the enhanced carrier collection [23–29].

In this study, we present a new type of photoanode consisting of a three-dimensional TiO_2 nanohelix (NH) array infiltrated with TiO_2 NPs (the NH-NP photoanode) for simultaneous improvements in the light-harvesting and the charge-collection efficiencies.

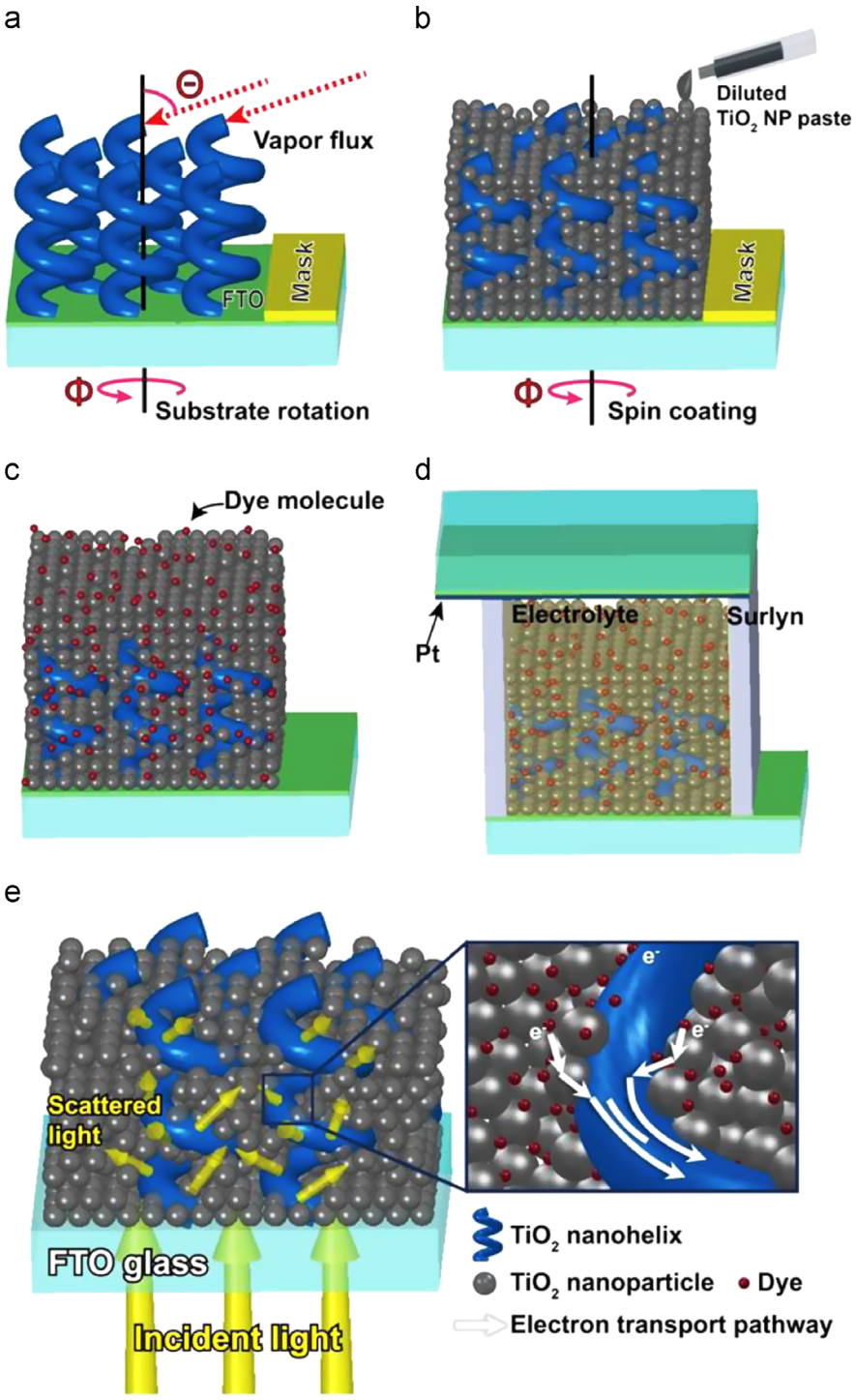

Fig. 1. Schematic illustrations of fabrication steps for a DSSC with TiO_2 NHs infiltrated with TiO_2 NPs; (a) formation of NH by oblique angle deposition with tilting angle of and rotating speed of Φ, (b) spin coating for infiltration of NPs into the empty spaces between the NHs, (c) dye adsorption, and (d) assembly of a sandwich type cell with a Pt coated counter electrode and injection of electrolyte. (e) Schematic description of light scattering and electron transport in a NH-NP photoanode. Incident light entering from the FTO glass substrate can be strongly scattered by the three-dimensional TiO_2 NHs, improving the light harvesting efficiency. The magnified view shows an enhanced transport of electrons generated from dye molecules, through the infiltrated TiO_2 NPs followed by a TiO_2 NH. Such a NH-NP photoanode can simultaneously improve the light harvesting and the carrier collection efficiency in photochemical cells including DSSCs.

The unique geometry of the vertically aligned TiO_2 NH array, fabricated by a facile method called oblique angle deposition, causes a strong light scattering effect as expected from the finite-element-method-based simulations. In addition, micro-structural analyses by X-ray diffraction (XRD) and high-resolution transmission electron microscopy (TEM) reveal near-single crystallinity of the TiO_2 NHs, resulting in strongly enhanced carrier transport. Consequently, the DSSC with the NH-NP photoanode shows an enhanced PCE despite much less dye loading than the DSSC with a conventional NP photoanode.

2. Fabrication of DSSCs

Fig. 1a–d shows the fabrication steps of a DSSC with a NH-NP photoanode. At first, the active region was defined on a FTO glass substrate by using a shadow mask, followed by the deposition of the TiO_2 NH array by oblique angle deposition [30,31]. A random fluctuation of the depositing material on the substrate at the initial stage of the oblique angle deposition produces shadow regions where subsequent incident vapor flux cannot reach, resulting in the creation of an array of slanted nanorods. By controlling the substrate rotation (Φ) as well as the vapor flux incidence angle (θ), a variety of three-dimensional arrays of nanostructures including NH can be fabricated in an easy, simple, and micro-fabrication-compatible way. For the formation of 3 μm-thick NH arrays on the active region (H3), the substrate was rotated while maintaining the oblique angle of 80° (Fig. 1a). Then, diluted TiO_2 NP paste with average diameter of 20 nm in ethanol was spin-coated on the NH arrays several times for infiltrating the empty space between the NHs with NPs (Fig. 1b). After infiltrating the 3 μm-thick NH arrays, additional 1 μm (H3P1) and 7 μm (H3P7) NP layers were added on top of the 3 μm NH-NP photoanodes by spin coating for a systematic investigation of various photoanodes. For comparison, DSSCs with conventional 10 μm-thick mesoporous NP layer (P10) having the same active layer thickness as the H3P7 sample was prepared as well. All the samples (H3, H3P1, H3P7, P10) were furnace-annealed at 500 °C for 30 min to form sintered networks of NPs and NH-NP, as well as to crystallize the as-grown amorphous TiO_2 NHs. Then, the samples were dyed in N719 dye ethanol solution (Fig. 1c) and a platinum deposited counter electrode was assembled to fabricate sandwich type DSSCs. Iodide/triiodide-based electrolyte was injected into the empty space between the two electrodes through holes on the counter electrode (Fig. 1d). More experimental details of the fabrication including the materials are described in the Supplementary material (S1). Fig. 1e shows a schematic description of how the NH-NP photoanode on a FTO substrate interacts with incident light to generate photocurrent efficiently. The TiO_2 NH array fulfils two important functions; scattering centers of the incident light and efficient pathways for photo-generated carriers while the infiltrated TiO_2 NPs provide a large surface area for dye adsorption. The enlarged view schematically shows how the NH-NP photoanode facilitates the efficient transport of electrons. Photo-generated electrons from dyes initially transport through the sintered network of TiO_2 NPs, and once entering a neighboring TiO_2 NH, the transport becomes much faster with much less probability of recombination than transport through a sintered network of TiO_2 NPs [32,33].

3. Results and discussion

Fig. 2a–d shows cross-sectional SEM images of the 3 μm NH array (H3), 3 μm NH-NP with additional 1 μm NP layer (H3P1), 3 μm NH-NP with additional 7 μm NP layer (H3P7), and the 10 μm NP-only layer (P10), respectively. As a consequence of the oblique angle deposition, an array of randomly distributed 3 μm-thick TiO_2 NHs was formed on the FTO glass substrate, as shown in Fig. 2a. Detail information on the dimension of the NHs and its possible effect on the performance of DSSCs are discussed in

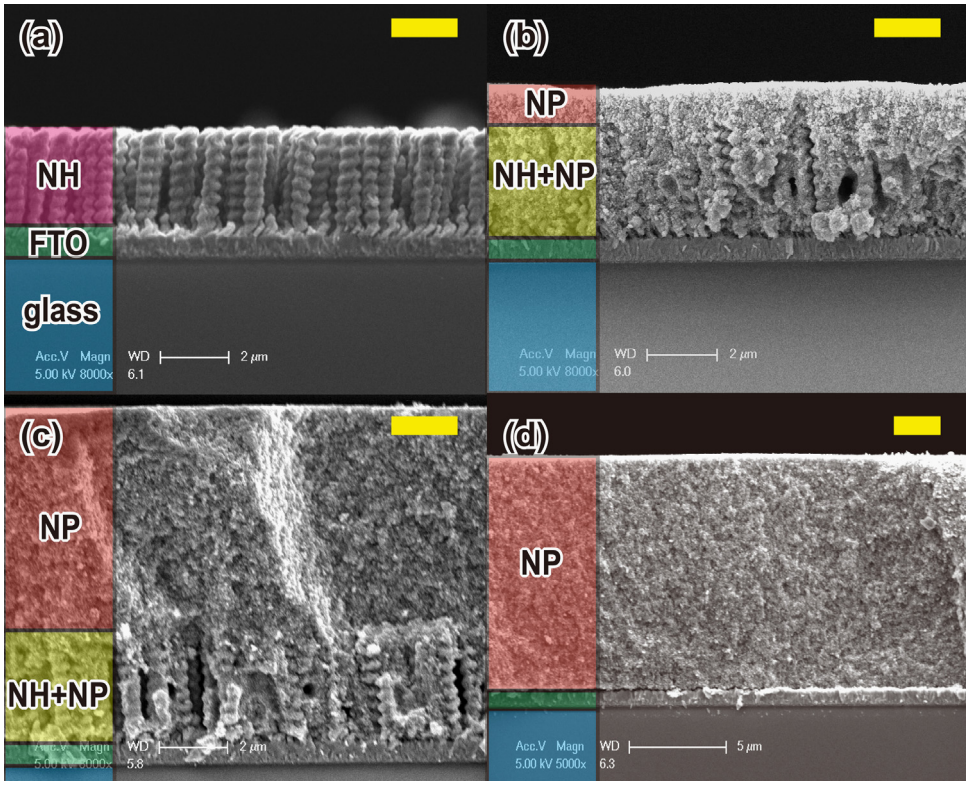

Fig. 2. Cross-sectional view of SEM images of the (a) 3 μm of NH array on FTO glass substrate (H3). (b, c) Combined photoanodes consist of infiltrated NH array with NPs with (b) additional 1 μm of NP layer (H3P1), (c) additional 7 μm of NP layer (H3P7), and (d) 10 μm of NP layer as reference. All scale bars indicate 2 μm.

Supplementary material (S2). The porosity of the 3 μm-thick NH film was estimated to be ~63% by using a linear effective medium approximation of the measured refractive index. Note that TiO_2 NPs can be penetrated into high density of empty spaces between NHs to form the NH-NP layer, mitigating the drawback of less surface area than NP-only layer (Fig. 2b and c). Some empty spaces between the NHs are shown in Fig. 2b, c because parts of the infiltrated NP have been chipped off during cleaving the samples for cross-sectional SEM measurements.

In order to compare the dye loading capacity of each photoanode, dye molecules attached on the photoanodes were desorbed and dissolved in a 0.1 M of NaOH solution [34], and the relative amount of dye molecules was estimated by measuring the absorption spectra of the dissolved solution as shown in Fig. 3. Dye molecules desorbed from the H3 shows the lowest absorption, and thus, the lowest dye adsorption density (1.85×10^{-8} mol/cm^2) among the photoanode samples, indicating that the surface area for dye adsorption is the smallest, as expected. As the surface area of photoanodes increases by infiltrating and overcoating NPs (H3P1 and H3P7), absorbance values, and hence dye adsorption densities (4.76×10^{-8} and 9.81×10^{-8} mol/cm^2) increase as well. The conventional NP photoanode (P10) shows the highest absorbance and dye adsorption density (1.61×10^{-7} mol/cm^2), indicating that conventional NP photoanode is superior to any other types of the photoanodes in terms of the dye loading capacity. Note that the H3P7 shows ~40% less dye adsorption density than the P10 despite the same thickness of active layer (10 μm). In order to achieve an enhanced PCE by using a nanostructured photoanode that offers improved charge collection efficiency, the vulnerable point in light harvesting caused by less dye loading should be mitigated or even overcome by a concomitant favorable optical effect, *e.g.*, enhanced light scattering.

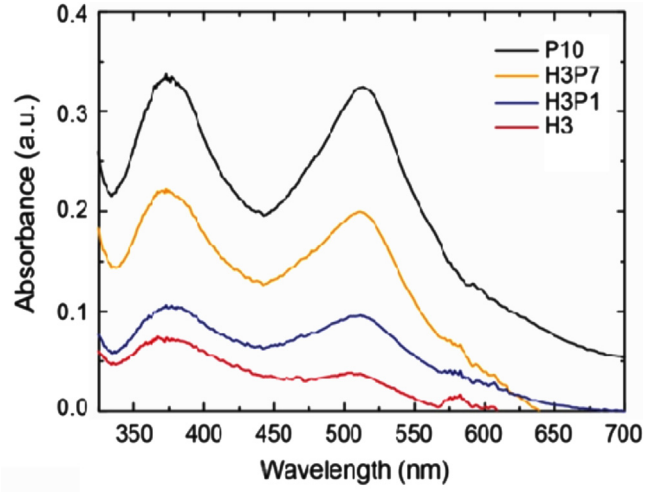

Fig. 3. Measured absorption spectra of dye molecules (N719) in 0.1 M NaOH solution desorbed from different photoanode structures.

It is expected that light scattering by three-dimensional nanostructures is much larger than that by a conventional NP layer and one-dimensional nanostructures. In order to estimate the effect of geometric shapes of photoanodes on light scattering, the light-propagation behaviors through various TiO_2 nanostructures were calculated by using commercial finite element method software (COMSOL Multiphysics). Details of the simulation are provided in the Supplementary material (S3). Fig. 4a–d shows the amplitude (in color scale) and the direction (black arrows) of the electric field at the surface of a vertically stacked NPs, a nanorod, a nanotube, and a NH when an x-polarized plane electromagnetic wave with 650 nm wavelength propagates from bottom to top (*i.e.* along the z-direction). For the conventional NP stack shown in Fig. 4a, the directions of scattered fields are nearly unchanged from the incident field – indicating that light scattering is negligible – and the amplitude of the electric fields is lower than for other nanostructures (Fig. 4b–e). The negligible light scattering for the NP stack is attributed to the size of TiO_2 NPs (typically ~20 nm), which is much smaller than the wavelength (λ) of incident light [8], while other structures having sizes comparable to λ. The combination of small NPs for high dye loading and large NPs for enhanced light scattering effect were reported [35,36], and it is fair to compare light scattering effect by nanostructures with similar dimension. Therefore, vertically stacked NPs with diameter of 150 nm comparable to that of the NH were also calculated (Fig. 4b). The highest amplitude of electric field and the most dynamic changes in the direction of scattered field are found in the three-dimensional NH (Fig. 4e), which is attributed to increased interface area between curled TiO_2 NHs and air where the incident light can be scattered - in other words, the light scattering cross-section for the NH array is much larger than that for larger size NPs stack and one-dimensional nanostructures. Video clips showing time-dependent propagation of electric fields

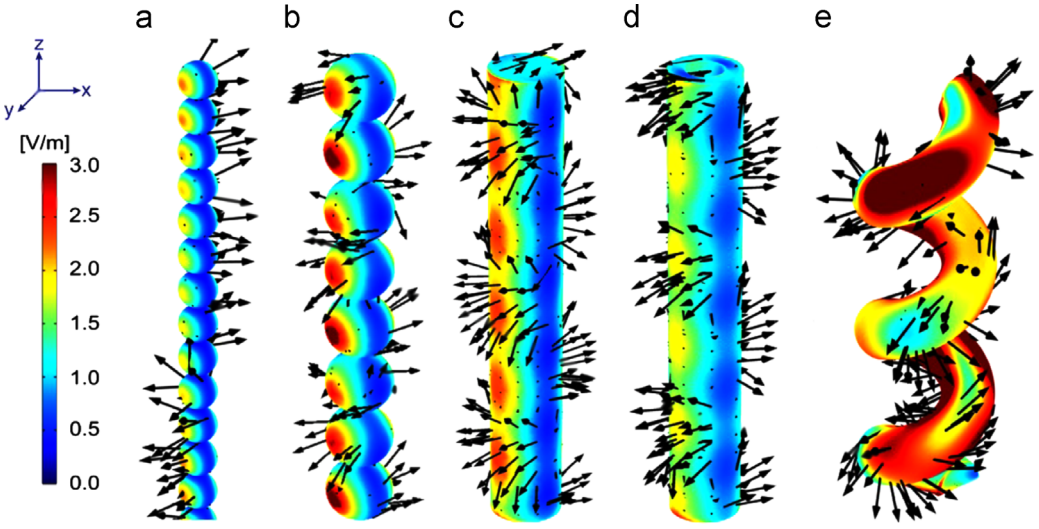

Fig. 4. The amplitude (in color scale) and the direction (black arrows) of the electric field at the surface of (a) a vertically stacked 20 nm size-NPs (magnified), (b) a vertically stacked larger size NPs (diameter of 150 nm), (c) a nanorod, (d) a nanotube, and (e) a NH when an x-polarized plane electromagnetic wave with 650 nm wavelength propagates from bottom to top (i.e. along the *z*-direction).

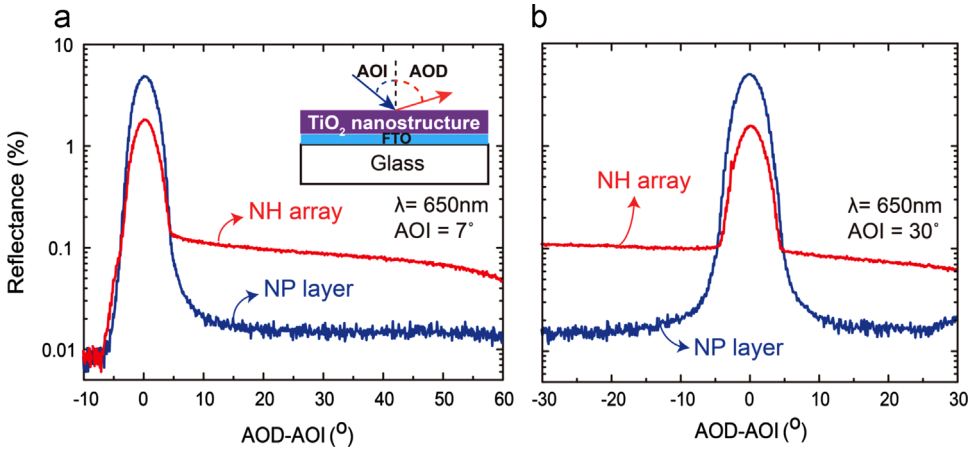

Fig. 5. Measured reflectance versus the difference between the angle of detector (AOD) and the angle of incidence (AOI) for the NP layer and the NH array samples with (a) AOI of 7° and (b) AOI of 30°. The inset shows schematic measurement configuration.

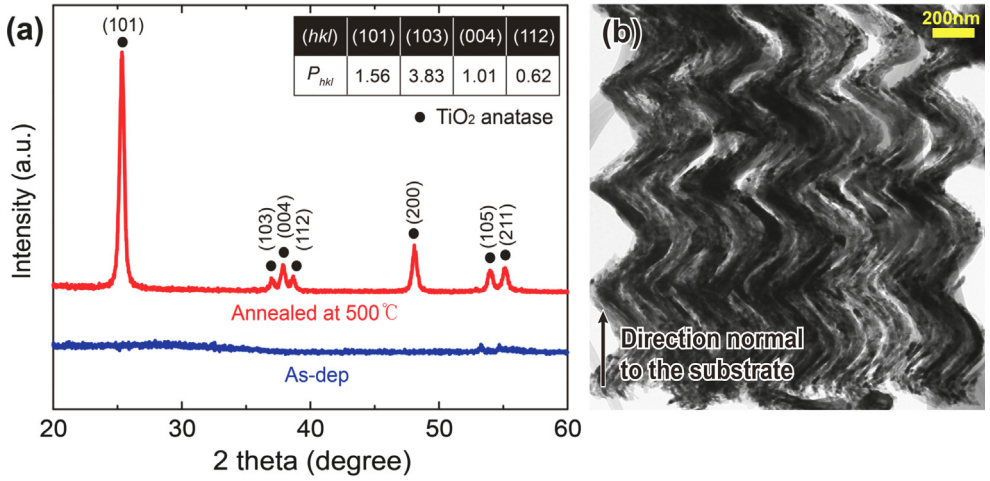

Fig. 6. (a) X-ray diffraction (XRD) patterns of as-deposited and annealed TiO_2 NH array. Calculated preferred orientations from the XRD data are shown in the inset. (b) TEM image of TiO_2 NHs array showing pronounced diffraction contrast.

through various photoanodes are presented in the Supplementary material (S3-a).

In order to experimentally verify the enhanced light scattering by the three-dimensional TiO_2 NH arrays, both diffuse and specular reflectance curves were measured, as shown in Fig. 5. The inset shows a schematic measurement configuration; monochromatic light (λ=650 nm) is incident on top of the NP layer and the NH array at two angles of incidence (AOI), 7° and 30°, and the reflected light is measured by scanning a photodetector as a function of angle of detection (AOD). Specular reflectance (when AOD ≈ AOI) of the NH array is lower while the diffuse reflectance of the NH array is much higher than that of the NP layer. Enhanced diffuse reflectance yet reduced specular reflectance indicates that the incident electromagnetic radiation spreads – *i.e.*, scatters – into wide range of directions by the three-dimensional NH array, consistent with the simulation results shown in Fig. 4. Such an enhanced light scattering by the photoanode increases the probability of the interaction between photons and dye molecules even in a very thin active layer, which allows one to use a thin active region for improving charge collection efficiency. In addition, the enhanced light scattering by the NH array can mitigate the poor dye adsorption caused by the small surface area for one- and three-dimensional nanostructured photoanodes, while maintaining the efficient transport property of photo-generated carriers.

Micro-structural properties of TiO_2 NHs were characterized by XRD and TEM. The XRD patterns of a TiO_2 NH array obtained before and after annealing are shown in Fig. 6a. No diffraction peak is observed in the XRD pattern of the as-deposited TiO_2 NHs, indicating that the TiO_2 NHs were deposited in the amorphous state. After annealing the TiO_2 NHs at 500 °C for 30 min, diffraction peaks appear in the XRD pattern, all of which can be indexed as those of the anatase phase of TiO_2. Fig. 6b presents a TEM image of the annealed TiO_2 NHs which shows pronounced diffraction contrast, indicating a high degree of crystallization. Note that the vertically aligned NHs remain stable after the crystallization process.

The preferred orientation of the anatase TiO_2 NHs was quantitatively evaluated from the XRD pattern by calculating

$$P = \frac{I(hkl)}{\sum I(hkl)} \frac{\sum I'(hkl)}{I'(hkl)}$$

where $I(hkl)$ is the measured peak intensity from (hkl) plane, and $I'(hkl)$ is the calculated peak intensity from the same plane of a randomly oriented powder sample [37]. The calculated P values, summarized in the inset of Fig. 6a, suggest that the preferred orientations of the vertical axis of NHs are ranked in the order of the (103), the (101), and the (004). Most of the anatase TiO_2 NHs investigated by TEM also revealed that the axis of helix is parallel

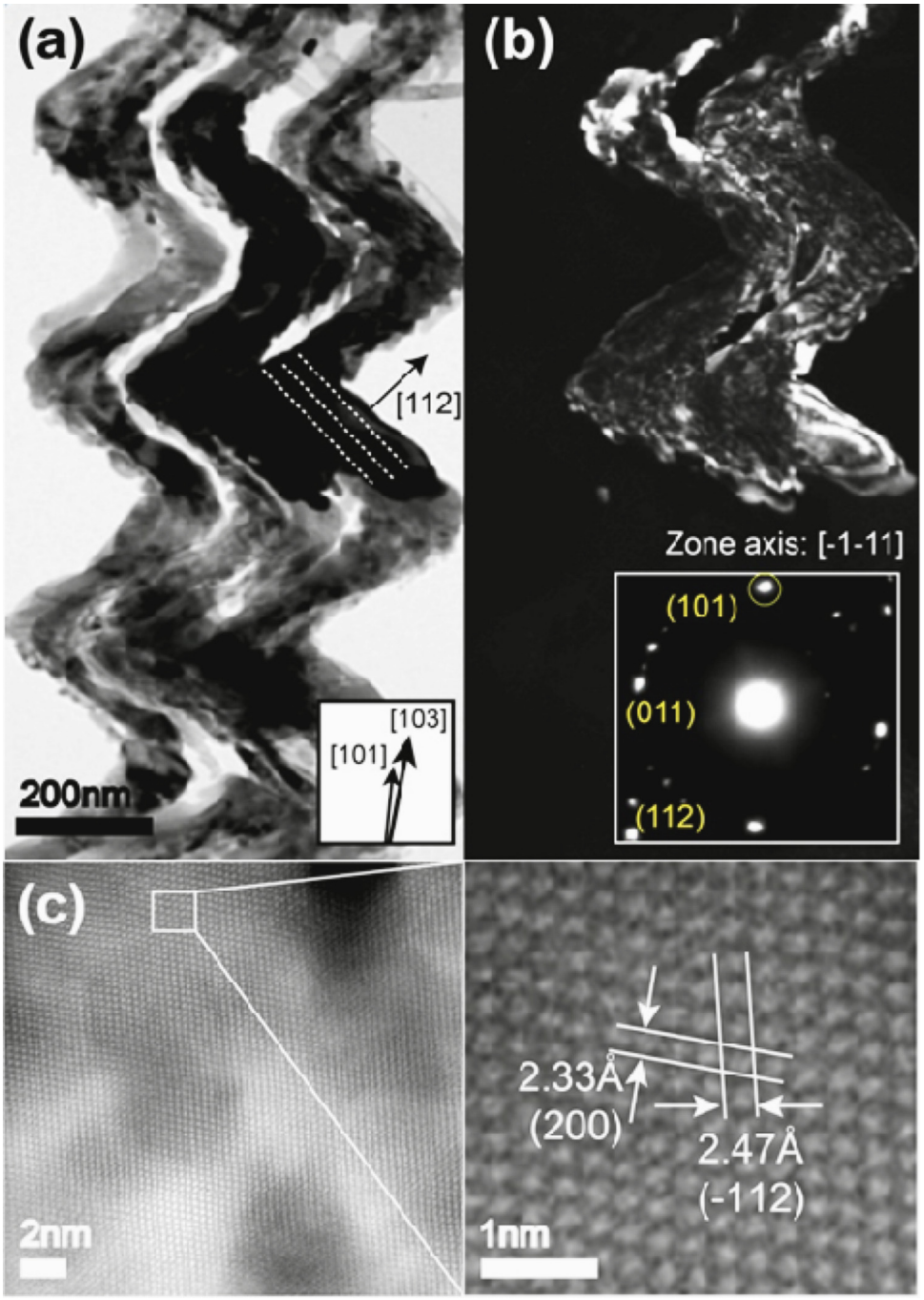

Fig. 7. (a) A bright field image of TiO_2 NHs after annealing. The dotted lines drawn parallel to the edge trace one of the possible planes estimated from the diffraction pattern shown in (b). The two major preferred orientations of NHs, the [101] and the [103], were shown in the inset. (b) A dark field image of the same NHs in (a) obtained by selecting the (101) diffracted beam. The $[-1-11]$ zone axis diffraction pattern is shown in the inset. (c) STEM-HAADF of the TiO_2 NH at low magnification (left) and a magnified view of the white-squared region (right) showing the lattice image of the anatase TiO_2.

to the [103] or the [101] (Fig. 7a), which agrees well with the XRD data.

Fig. 7a and b shows a pair of bright-field and dark-field TEM images of TiO_2 NHs. While small granular contrast is observed along the edges of NHs, large grains spanning over ~500 nm are frequently observed along the axis of NHs. The dark-field image formed by using the (101) diffracted beam highlights such a large grain. We investigated many NHs and observed the existence of such large grains in most of the NHs. (See Supplementary material S4) Interestingly, the average grain size along the axis of helix was comparable to 1.5 pitches of the helix, where one pitch corresponds to 413 ± 25 nm. Fig. 7c shows a high-angle annular dark-field scanning TEM (HAADF-STEM) image recorded at the edge of such a large grain. The atomic columns are clearly resolved, demonstrating the high crystallinity of such large grains in TiO_2 NHs. The large grain size coupled with the near-single crystallinity of TiO_2 NHs ensures that the carrier transport through such TiO_2 NHs can be enhanced significantly in comparison with that through a network of NPs where the grain boundaries between NPs act as recombination and scattering centers for carrier transport.

In order to investigate the contribution of the NH array to the electron transport properties in the NH-NP photoanodes, we evaluated the electron transport time and electron diffusion

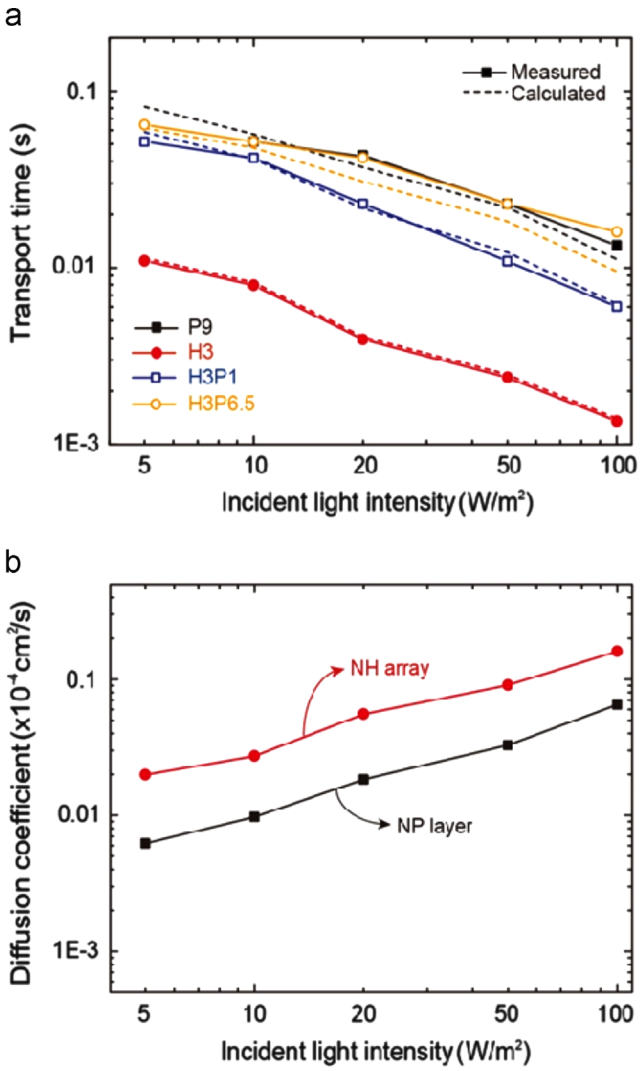

Fig. 8. (a) Electron transport time and (b) electron diffusion coefficients (D_n) of various photoanodes estimated by analyzing intensity modulated photocurrent spectroscopy data acquired under the illumination of a 530 nm light source with varying light intensities from 5 to 100 W/m^2. Calculated results based on our analytic electron transport model are shown by dotted lines in (a).

coefficients (D_n) by analyzing intensity modulated photocurrent spectroscopy data acquired under the illumination of a 530 nm light source with varying light intensities from 5 to 100 W/m^2. Symbols in Fig. 8a show measured electron transport time of various photoanodes as a function of the incident light intensity. The H3 sample shows much shorter electron transport time than the NH-NP and conventional NP photoanodes, because photo-generated electrons transport only through near-single crystalline NHs with much less grain boundaries than other photoanodes containing an entangled network of NPs. As the amount of TiO_2 NPs increases by infiltrating and overcoating additional TiO_2 NPs, the electron transport time becomes longer and approaches the values of the conventional NP-only photoanode. Fig. 8b shows that diffusion coefficient (D_n) calculated by $D_n = d^2/4\tau_c$ [30,38] where d is the thickness of film in which electrons travel and τ_c is electron transport time. The diffusion coefficient in the NH array is more than 3 times higher than that in the NP layer, showing much enhanced carrier transport along the near-single crystalline TiO_2 NHs. In addition, electrochemical impedance spectroscopy result showing the enhanced performance of carrier transportation is provided in Supplementary material (S5). In order to elucidate the mechanism of electron transport in NH-NP photoanodes, we

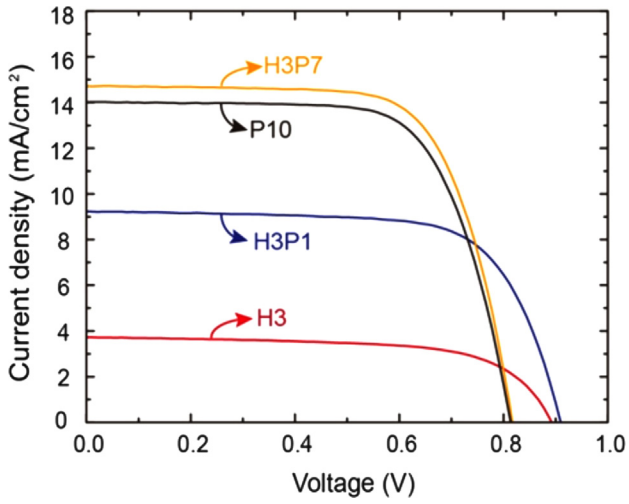

Fig. 9. Photocurrent-density-versus-voltage (J–V) curves for the DSSCs with various photoanodes measured under AM1.5 illumination at the radiation intensity of 100 mW/cm^2.

Table 1
Photovoltaic performances of the DSSCs with various photoanodes estimated from the J–V curves in Fig. 9.

	Total thickness (μm)	J_{sc} (mA/cm^2)	V_{oc} (V)	*FF* (%)	PCE (%)
H3	3	3.72	0.89	65.65	2.17
H3P1	4	9.23	0.91	70.02	5.87
H3P7	10	14.72	0.82	69.88	8.40
P10	10	14.03	0.81	72.84	7.91

developed an analytic model to estimate the transport time. Details of the model are described in Supplementary material (S6). The dotted lines in Fig. 8a show calculated transport times with incident light intensity based on our analytic model for each photoanode, very consistent with experimentally obtained transport times. As the thickness of overcoated TiO_2 NPs increases, the electron transport time approaches the values of the NP-only photoanode, indicating that the transport-rate-determining step in the NH-NP photoanodes is the transport through the entangled network of NPs. This result provides a clue for further improvement in transport properties of NH-NP photoanodes; for example, H10P0 - a NH-NP photoanode with 10 μm NH array infiltrated with NPs will lead to much faster transport time than the H3P7 because the average traveling length for photo-generated carriers to the NH array should be much shorter while maintaining the enhancement in light harvesting.

Fig. 9 shows the photocurrent-density-versus-voltage (J–V) curves for the DSSCs with various photoanodes measured under AM1.5 illumination at the radiation intensity of 100 mW/cm^2. The photovoltaic performances are summarized in Table 1. The open circuit voltages (V_{oc}) of the DSSCs with the H3 and H3P1 are higher than that with P10 and H3P7 because thinner total thickness of the photoanodes leads to a lower number of trapping surface states [39]. Additionally, V_{oc} of DSSCs with H3 photoanode is as high as 0.89 V due to the low charge recombination from improved diffusion coefficient and small mass transport resistance in thin and open structured film [40], however, the short circuit current density (J_{sc}) is very low (3.72 mA/cm^2) due to its small surface area, resulting in the lowest PCE (2.17%) among the samples. The J_{sc} values are increased to 9.23 mA/cm^2 and 14.72 mA/cm^2 for the H3P1 and the H3P7 samples, respectively, indicating that increased surface area of NH-NP photoanodes enhances the capability of light harvesting, which consequently results in improved PCEs (5.87% and 8.40%). Note that the DSSC with H3P7

shows 4.9% higher J_{sc} and 6.2% higher PCE than the conventional DSSC with P10 photoanode despite ~40% lower dye adsorption. Enhanced light scattering by the array of three-dimensional NHs, which has been proved by both simulations and experiments, together with comparable surface area with NP photoanode by infiltrating and overcoating NPs results in an enhanced light harvesting, and hence, higher J_{sc}. In addition, the diffusion coefficient through the NH array is more than 3 times higher than that through the NP layer, which is attributed to the large grains constituting the NHs together with their near-single crystallinity. Therefore, a remarkable reduction in carrier transport time through such TiO_2 NHs is expected compared to an entangled network of NPs with a large number of grain boundaries between small NPs. However, as the thickness of over coated NP layer increases in a NH-NP photoanode – for example, H3P7 – the total electron transport time is mainly determined by the time through the network of the thick NP layer, approaching the long transport time in the NP-only photoanode. Therefore, the improvement in the PCE of the DSSCs with H3P7 is mainly attributed to the enhanced light harvesting rather than promoted carrier transport by the array of NHs. It should be noted that there is great room for further improvement in PCE of DSSCs by taking advantage of the excellent transport properties as well as the light scattering effect by appropriate design and optimization of NH-NP photoanodes, for example, H10P0, as expected from our analytic model (please see S6).

4. Conclusions

In summary, we developed a new type of photoanode based on the arrays of three-dimensional near-single crystalline TiO_2 NHs – fabricated by the oblique angle deposition method – infiltrated with TiO_2 NPs – easily fabricated by spin coating - pursuing simultaneously improvements in the light harvesting and the charge collection efficiencies of DSSCs. The NH-NP photoanode based DSSCs, despite ~40% less dye loading, show 6.2% higher PCE than DSSCs with conventional NP photoanode. This improvement is attributed to the unique geometry of a three-dimensional NH array photoanode causing significant light scattering for much enhanced light harvesting. In addition, infiltrated TiO_2 NPs provide a large surface area for the adsorption of dye molecules. We believe that there is much room for further improvement in PCE by optimization of length of NHs and the amount of infiltrated NPs for more efficient electron transport, *i.e.*, by eliminating trade-off between the light harvesting and the carrier collection. Furthermore, the proposed photoanode concept can be also applied to photoelectrochemical cells for water splitting and artificial photosynthesis, organic photovoltaic devices, *etc.*, in which simultaneous improvements in light harvesting and charge collection are important, leading to significant technical progress in a wide range of optoelectronic devices.

Acknowledgments

Seung Hee Lee and Jeong Kwon contributed equally to this work. The authors gratefully acknowledge supports by Global Research Network program (2011-220-D00064) funded by the National Research Foundation of Korea (NRF), and by POSCO Fusion Technology Center for Materials.

Appendix A. Supplementary material

Supplementary data associated with this article can be found in the online version at http://dx.doi.org/10.1016/j.solmat.2014.08.007.

References

[1] B. O'Regan, M. Grätzel, A low-cost, high-efficiency solar cell based on dye-sensitized colloidal TiO_2 films, Nature 353 (1991) 737–740.
[2] A. Hagfeldt, G. Boschloo, L. Sun, L. Kloo, H. Pettersson, Dye-sensitized solar cells, Chem. Rev. 110 (2010) 6595–6663.
[3] C. Prasittichai, J.T. Hupp, Surface modification of SnO_2 photoelectrodes in dye-sensitized solar cells: significants improvements in photovoltage via Al_2O_3 atomic layer deposition, J. Phys. Chem. Lett. 1 (2010) 1611–1615.
[4] M. Grätzel, Solar energy conversion by dye-sensitized photovoltaic cells, Inorg. Chem. 44 (2005) 6841–6851.
[5] F. Pichot, J. Pitts, B. Gregg, Low-temperature sintering of TiO_2 colloids: application to flexible dye-sensitized solar cells, Langmuir 16 (2000) 5626–5630.
[6] A. Yella, H.-W. Lee, H.N. Tsao, C. Yi, A.K. Chandiran, M.K. Nazeeruddin, E.W.G. Diau, C.-Y. Yeh, S.M. Zakeeruddin, M. Grätzel, Porphyrin-sensitized solar cells with cobalt (II/III)-based redox electrolyte exceed 12 percent efficiency, Science 334 (2011) 629–634.
[7] H.J. Snaith, Estimating the maximum attainable efficiency in dye-sensitized solar cells, Adv. Funct. Mater. 20 (2010) 13–19.
[8] Q. Zhang, D. Myers, J. Lan, S.A. Jenekhe, G. Cao, Applications of light scattering in dye-sensitized solar cells, Phys. Chem. Chem. Phys. 14 (2012) 14982–14992.
[9] S.H. Kang, S.H. Choi, M.S. Kang, J.Y. Kim, H.S. Kim, T. Hyeon, Y.E. Sung, Nanorod-based dye-sensitized solar cells with improved charge collection efficiency, Adv. Mater. 20 (2008) 54–58.
[10] K. Zhu, T.B. Vinzant, N.R. Neale, A.J. Frank, Removing structural disorder from oriented TiO_2 nanotube arrays: reducing the dimensionality of transport and recombination in dye-sensitized solar cells, Nano Lett. 7 (2007) 3739–3746.
[11] B. Liu, E.S. Aydil, Growth of oriented single-crystalline rutile TiO_2 nanorods on transparent conducting substrates for dye-sensitized solar cells, J. Am. Chem. Soc. 131 (2009) 3985–3990.
[12] J. Nelson, Continuous-time random-walk model of electron transport in nanocrystalline TiO_2 electrodes, Phys. Rev. B 59 (1999) 15374–15380.
[13] M. Law, L.E. Greene, J.C. Johnson, R. Saykally, P. YangNanowire dye-sensitized solar cells 4 (2005) 455–459Nat. Mater. 4 (2005) 455–459.
[14] X. Feng, K. Zhu, A.J. Frank, C.A. Grimes, T.E. Mallouk, Rapid charge transport in dye-sensitized solar cells made from vertically aligned single-crystal rutile TiO_2 nanowires, Angew. Chem. 124 (2012) 2781–2784.
[15] X. Feng, K. Zhankar, O.K. Varghese, M. Paulose, T.J. Latempa, C.A. Grimes, Vertically aligned single crystal TiO_2 nanowire arrays grown directly on transparent conduction oxide coated glass: synthesis details and applications, Nano Lett. 8 (2008) 3781–3786.
[16] J.B. Baxter, E.S. Aydi, Nanowire-based dye-sensitized solar cells, Appl. Phys. Lett. 86 (2005) 053114.
[17] E. Galoppini, J. Rochford, H. Chen, G. Saraf, Y. Lu, A. Hagfeldt, G. Boschloo, Fast electron transport in metal organic vapor deposition grown dye-sensitized ZnO nanorod solar cells, J. Phys. Chem. B 110 (2006) 16159–16161.
[18] M. Wang, J. Bai, F.L. Formal, S.J. Moon, L.C. Ha, R.H. Baker, C. Grätzel, S.M. Zakeeruddin, M. Grätzel, Solid-state dye-sensitized solar cells using ordered TiO_2 nanorods on transparent conductive oxide as photoanodes, J. Phys. Chem. C 116 (2012) 3266–3273.
[19] K. Zhu, N.R. Neale, A. Miedaner, A.J. Frank, Enhanced charge-collection efficiencies and light scattering in dye-sensitized solar cells using oriented TiO_2 nanotubes arrays, Nano Lett. 7 (2007) 69–74.
[20] G.K. Mor, K. Shankar, M. Paulose, O.K. Varghese, C.A. Grimes, Use of highly-ordered TiO_2 nanotube arrays in dye-sensitized solar cells, Nano Lett. 6 (2006) 215–218.
[21] S. Lee, I.J. Park, D.H. Kim, W.M. Sung, D.W. Kim, G.S. Han, J.Y. Kim, H.S. Jung, K.S. Hong, Crystallographically preferred oriented TiO_2 nanotube arrays for efficient photovoltaic energy conversion, Energy Environ. Sci. 5 (2012) 7989–7995.
[22] A.B.F. Martinson, J.W. Elam, J.T. Hupp, M.J. Pellin, ZnO nanotube based dye-sensitized solar cells, Nano Lett. 7 (2007) 2183–2187.
[23] S.H. Ko, D. Lee, H.W. Kang, K.H. Nam, J.Y. Yeo, S.J. Hong, C.P. Grigoropoulos, H.J. Sung, Nanoforest of hydrothermally grown hierarchical ZnO nanowires for a high efficiency dye-sensitized solar cells, Nano Lett. 11 (2011) 666–671.
[24] Y. Bai, H. Yu, Z. Li, R. Amal, G.Q. Lu, L. Wang, In-situ growth of a ZnO nanowire network within a TiO_2 nanoparticle film for enhanced dye-sensitized solar cell performance, Adv. Mater. 24 (2012) 5850–5856.
[25] Q. Zheng, H. Kang, J. Yun, J. Lee, J.H. Park, S. Baik, Hierarchical construction of self-standing anodized titania nanotube arrays and nanoparticles for efficient and cost-effective front-illuminated dye-sensitized solar cells, ACS Nano 5 (2011) 5088–5093.
[26] M. McCune, W. Zhang, Y. Deng, High efficiency dye-sensitized solar cells based on three-dimensional multilayered ZnO nanowire arrays with "caterpillar-like" structure, Nano Lett. 12 (2012) 3656–3662.
[27] M. Ye, D. Zheng, M. Lv, C. Chen, C. Lin, Z. Lin, Hierarchically structured nanotubes for highly efficient dye-sensitized solar cells, Adv. Mater. 25 (2013) 3039–3044.
[28] I. Herman, J. Yeo, S. Hong, D. Lee, K.H. Nam, J. Choi, W. Hong, D. Lee, C.P. Grigoropoulos, S.H. Ko, Hierarchical weeping willow nano-tree growth and effect of branching on dye-sensitized solar cell efficiency, Nanotechnology 23 (2012) 194005.

[29] D. Lee, Y. Rho, F.I. Allen, A.M. Minor, S.H. Ko, C.P. Grigoropoulos, Synthesis of hierarchical TiO_2 nanowires with densely-packed and omnidirectional branches, Nanoscale 5 (2013) 11147–11152.
[30] M.M. Hawkeye, M.J. Brett, Glancing angle deposition: fabrication, properties, and applications of micro- and nanostructured thin films, J. Vac. Sci. Technol. A 25 (2007) 1317–1335.
[31] K. Robbie, M.J. Brett, Sculptured thin films and glancing angle deposition: growth mechanics and applications, J. Vac. Sci. Technol. A 15 (1997) 1460–1465.
[32] J. van de Lagemaat, A.J. Frank, Nonthermalized electron transport in dye-sensitized nanocrystalline TiO_2 films: transient photocurrent and random-walk modeling studies, J. Phys. Chem. B 105 (2001) 11194–11205.
[33] C. Kang, Y. Xie, E. Xie, Enhanced photovoltaic characterization of TiO_2 nanoparticle/nanotube composite film based on dye-sensitized solar cells and charge-transport mechanism discussion, J. Optoelectron. Adv. Mater. 5 (2011) 518–522.
[34] Y.-C. Park, Y.-J. Chang, B.-G. Kim, E.-H. Kong, J.Y. Son, Y.S. Kwon, T. Park, H. M. Jang, Size-tunable mesoporous spherical TiO_2 as a scattering overlayer in high-performance dye-sensitized solar cells, J. Mater. Chem. 21 (2011) 9582–9586.
[35] D. Hwang, H. Lee, Y. Seo, D. Kim, S.M. Jo, D.Y. Kim, Enhanced charge collection efficiency of dye-sensitized solar cells based on size-tunable hierarchically structured TiO_2 beads, J. Mater. Chem. A 1 (2013) 1359–1369.
[36] Y. Rho, M. Wanit, J. Yeo, S. Hong, S. Han, J.-H. Choi, W.-H. Hong, D. Lee, S.H. Ko, Improvement of light-harvesting efficiency in dye-sensitized solar cells using silica beads embedded in a TiO_2 nanoporous structure, J. Phys. D: Appl. Phys. 46 (2013) 024006.
[37] D. Brandon, W.D. Kaplan, Microstructural characterization of materials, second ed., Wiley, New York, 2008.
[38] N.G. Park, J. van de Lagemaat, A. Frank, Effect of morphology on electron transport in dye-sensitized nanostructured TiO_2 films, J. Photosci. 10 (2003) 199–202.
[39] M.G. Kang, K.S. Ryu, S.H. Chang, N.G. Park, J.S. Hong, K.-J. Kim, Dependence of TiO_2 film thickness on photocurrent-voltage characteristics of dye-sensitized solar cells, Bull. Korean Chem. Soc. 25 (2004) 742–744.
[40] Z.–S. Wang, H. Kawauchi, T. Kashima, H. Arakawa, Significant influence of TiO_2 photoelectrode morphology on the energy conversion efficiency of N719 dye-sensitized solar cell, Coord. Chem. Rev. 248 (2004) 1381–1389.